IEEE Robotics and Automation Letters (RA-L) paper, presented at ICRA 2026, Vienna, Austria. Cite as RA-L paper.

Cosserat Rods with Cross-Sectional Deformation for Soft Robot Modeling

Samuel Tobin[1], *Graduate Student Member, IEEE,* Joshua Gaston[1], Vincent Aloi[2], Eric Barth[3], *Member, IEEE,* Caleb Rucker[1], *Senior Member, IEEE*

***Abstract*—Cosserat rod models are widely used to simulate, design, and control soft robots. The Cosserat framework accounts for bending, torsion, transverse shear, and elongation of a long, slender structure and correctly handles large rotations and deflections in 3D, while being far less computationally expensive than full 3D elasticity models using finite elements. However, the Cosserat model is not always appropriate for soft robotic structures since it assumes the cross sections never change size or shape. In this letter, we extend the standard Cosserat rod model to include cross-sectional deformation while retaining much of its simplicity. We add to the Cosserat model additional degrees of freedom that parameterize stretch and shear in the cross-sectional plane and their rates of change along the rod length. We then formulate several possible constitutive laws on the state variables (one linear and one non-linear) and compare them to the standard Cosserat energy expressions to gain insight. We further show how fluidic actuation and tendon actuation can be incorporated into the model, and we compare the extended Cosserat models to 3D nonlinear finite-element simulations with good agreement. Finally, we demonstrate use of this model in a robotics context to control the path-following gait of a peristaltic worm-inspired soft robot.**

***Index Terms*—Modeling, Control, and Learning for Soft Robots, Simulation and Animation**

I. Introduction and Background

A. Related Work

ROD theories have demonstrated their utility across a wide range of fields, including soft robotics, carbon nanotubes, biomechanics, and computer graphics [1]–[5]. Unlike traditional volumetric approaches, which characterize all three spatial dimensions of a structure, rod theories assume the structure is slender and, therefore, can be treated as an object with only one material dimension along the length parameterized by s with each material frame equipped with a rigid cross-section [6], [7]. This reduction in dimensionality significantly improves computational efficiency by decreasing the number of degrees of freedom [8]. As a result, for slender objects, such as some soft and continuum robots, these rod models have become exceedingly popular [9]–[11].

The most comprehensive of the rod theories, known as Cosserat rod theory [12], considers bending, twisting, shearing, and stretching. It describes the material frame using three orthonormal vectors called directors and employs a rigid cross section assumption [6], [13], [14]. However, the rigid cross-section assumption may not hold for non-slender geometries or highly incompressible materials in which Poisson effects are significant, or soft robots actuated by a pneumatic or hydraulic system [15]. In these cases, assuming a rigid cross section can lead to inaccuracy [16]. This has motivated research into computationally efficient mechanics based models to account for cross-sectional deformation.

Tunay [9] introduces a rod model that uses non-unit quaternions to parameterize inflation for soft robots, but not other kinds of cross section deformation. For thin-walled structures, wall-deformation has been addressed using geometrically exact finite elements for plates and shell models [17], [18]. However, shell and plate theory involves modeling two material dimensions, resulting in an increased computational cost. Thus, in [19], [20], the cross-sectional deformation of thin-walled elongated structures (beams and hollow tubes) are modeled more efficiently by extending one-dimensional beam theory with thin-walled modes. To model more general deformations throughout the material cross section, Rubin showed in [21] that the orthonormal restriction on the Cosserat rod directors can be relaxed, such that the directors are only linearly dependent with each other. This allows for cross-sectional stretch and shear. In [22] a mixed finite element formulation is shown to model cross-sectional deformation by a St. Venant constitutive law, and [23] included general in-plane cross-sectional deformation and out-of-plane warping. Recently, [24], [25] extended Cosserat rod theory to allows for cross-sectional deformation by defining three field variables to capture isotropic stretching and shearing of a rod's cross section. Objective strain measures were used to characterize the energy of the system. This approach was further applied to carbon nanotubes [26] and extended to general constitutive laws consistent with nonlinear elasticity in [16].

B. Contributions

In this letter we seek to advance the prior work in this area toward applications in continuum and soft robotics. We start with the same basic assumptions as [24], [25], but our

Manuscript received: April 30, 2025; Revised August 8, 2025; Accepted September 16, 2025.

This paper was recommended for publication by Editor Cecilia Laschi upon evaluation of the Associate Editor and Reviewers' comments.

Parts of this work are based upon work supported by the National Science Foundation under EFMA-1935278 and under NSF CAREER Award IIS-1652588. Any opinion, findings, and conclusions or recommendations expressed herein are those of the authors and do not necessarily reflect the views of the National Science Foundation.

[1] Samuel Tobin, Joshua Gaston, and Caleb Rucker are with the Department of Mechanical & Aerospace Engineering, University of Tennessee-Knoxville, Knoxville, TN, USA

[2] Vincent Aloi is with the Department of Robotics Engineering, Worcester Polytechnic Institute, Worcester, MA, USA

[3] Eric Barth is with the Department of Mechanical Engineering, Vanderbilt University, Nashville, TN, USA

Digital Object Identifier (DOI): see top of this page.

IEEE Robotics and Automation Letters (RA-L) paper, presented at ICRA 2026, Vienna, Austria. Cite as RA-L paper.

development further identifies the individual coefficients in the energy density in terms of standard material parameters. In the process, we identify some new coupling terms that did not appear in prior work. We also develop several versions of the extended Cosserat elastic energy density (linearized, nonlinear, and with additional modes), and we show how and why to incorporate bending and torsion stiffness modifications for greater accuracy, especially for nearly incompressible materials. We then show how to implement these models with an energy minimization approach, including soft robot actuation through tendon tension or fluid pressure. Simulations using the various models are then compared to reference nonlinear finite element simulations to verify the results in cases of axial extension, bending, and torsion.

II. Geometric Framework and Constitutive Laws

A. Parameterizing the Deformation

Following the work of Kumar [24], we write the global cartesian position $\mathbf{x} \in \mathbb{R}^3$ of a material point as a function of its position $\mathbf{X} = [x\ y\ s]^\top$ in the stress-free reference configuration, where s is the reference arc length along the rod, and x and y denote 2D cartesian coordinates within the cross-sectional slice at s. The deformation is written as

$$\mathbf{x}(x, y, s) = \mathbf{p}(s) + \mathbf{R}(s)\mathbf{C}(s)\mathbf{r}(x, y) \tag{1}$$

where $\mathbf{p}(s) \in \mathbb{R}^3$ is the position of the cross section center at reference arc length s,

$$\mathbf{r} = [x\ y\ 0]^\top \tag{2}$$

is the position of the material point in the reference cross section, $\mathbf{C} \in \mathbb{R}^{3\times3}$ is a matrix performing a symmetric linear transformation on the cross section material in its own plane

$$\mathbf{C}(s) = \begin{bmatrix} a(s) & c(s) & 0 \\ c(s) & b(s) & 0 \\ 0 & 0 & 1 \end{bmatrix} \tag{3}$$

with a and b corresponding to cross-sectional stretching and c corresponding to cross-sectional shearing. $\mathbf{R} \in \mathrm{SO}(3)$ is a rotation matrix describing the orientation of the cross-sectional slice. We further define $\mathbf{v} \in \mathbb{R}^3$ and $\mathbf{u} \in \mathbb{R}^3$ as

$$\begin{aligned} \frac{\partial \mathbf{p}}{\partial s} &= \mathbf{p}' = \mathbf{R}\mathbf{v} \\ \frac{\partial \mathbf{R}}{\partial s} &= \mathbf{R}' = \mathbf{R}\widehat{\mathbf{u}} \end{aligned} \tag{4}$$

as in the conventional Cosserat model, and note that we will use $'$ to denote differentiation with respect to s throughout. The deformation gradient associated with the parameterized displacement field can then be written as

$$\begin{aligned} \mathbf{F} &= \frac{\partial \mathbf{x}}{\partial \mathbf{X}} = \begin{bmatrix} \frac{\partial \mathbf{x}}{\partial x} & \frac{\partial \mathbf{x}}{\partial y} & \frac{\partial \mathbf{x}}{\partial s} \end{bmatrix} \\ &= \mathbf{R}\begin{bmatrix} \mathbf{C}\mathbf{e}_1 & \mathbf{C}\mathbf{e}_2 & \mathbf{v} + \widehat{\mathbf{u}}\mathbf{C}\mathbf{r} + \mathbf{C}'\mathbf{r} \end{bmatrix} = \mathbf{R}\mathbf{D} \end{aligned} \tag{5}$$

where $\mathbf{e}_1$, $\mathbf{e}_2$ and $\mathbf{e}_3$ are the standard bases in $\mathbb{R}^3$. As shown above, the rotation $\mathbf{R}$ can be factored out of $\mathbf{F}$, and the remaining factor $\mathbf{D}$ describes the part of the deformation that is independent of rigid-body rotation. As such, the terms of $\mathbf{D}$ can be used to formulate an objective strain measure, similar to that obtained from a polar decomposition of $\mathbf{F}$, but not identical to it since $\mathbf{D}$ is not symmetric. In terms of the parameters of the deformation, and the reference position (x, y, s), $\mathbf{D}$ is

$$\mathbf{D} = \begin{bmatrix} a & c & v_1 + a'x + c'y - bu_3y - cu_3x \\ c & b & v_2 + b'y + c'x + au_3x + cu_3y \\ 0 & 0 & v_3 - (au_2 - cu_1)x + (bu_1 - cu_2)y \end{bmatrix} \tag{6}$$

where a, b, c, $\mathbf{u}$, and $\mathbf{v}$ are all implicit functions of s.

B. Constitutive Law with Linearization

Now departing from the work of Kumar [24], we will construct constitutive laws based on linear elasticity in the rotated cross section frame. Our approach is essentially a co-rotational or St. Venant- Kirchhoff approach, but we will explore two variants: one which linearizes $\mathbf{D}$ and results in quadratic strain energy, and a second which leaves $\mathbf{D}$ nonlinear and results in a higher order energy expression. Exploring the simpler case first to build intuition, we linearize $\mathbf{D}$ with respect to $\mathbf{u}$ and $\mathbf{C}$ about the reference configuration ($\mathbf{u} = \mathbf{0}$ and $\mathbf{C} = \mathbf{I}$), which replaces $\widehat{\mathbf{u}}\mathbf{C}$ with $\widehat{\mathbf{u}}$),

$$\begin{aligned} \mathbf{D} &\approx \begin{bmatrix} \mathbf{C}\mathbf{e}_1 & \mathbf{C}\mathbf{e}_2 & \mathbf{v} + \widehat{\mathbf{u}}\mathbf{r} + \mathbf{C}'\mathbf{r} \end{bmatrix} \\ &\approx \begin{bmatrix} a & c & v_1 + a'x + c'y - u_3y \\ c & b & v_2 + b'y + c'x + u_3x \\ 0 & 0 & v_3 - u_2x + u_1y \end{bmatrix} \end{aligned} \tag{7}$$

The symmetric strain tensor in the rotated frame is then

$$\boldsymbol{\epsilon} = \begin{bmatrix} \epsilon_{xx} & \frac{\gamma_{xy}}{2} & \frac{\gamma_{xz}}{2} \\ \frac{\gamma_{xy}}{2} & \epsilon_{yy} & \frac{\gamma_{yz}}{2} \\ \frac{\gamma_{xz}}{2} & \frac{\gamma_{yz}}{2} & \epsilon_{zz} \end{bmatrix} = \frac{1}{2}(\mathbf{D} + \mathbf{D}^\top) - \mathbf{I}. \tag{8}$$

resulting in the strain vector

$$\underline{\boldsymbol{\epsilon}} = \begin{bmatrix} \epsilon_{xx} \\ \epsilon_{yy} \\ \epsilon_{zz} \\ \gamma_{yz} \\ \gamma_{xz} \\ \gamma_{xy} \end{bmatrix} = \begin{bmatrix} a - 1 \\ b - 1 \\ v_3 - u_2x + u_1y - 1 \\ v_2 + b'y + c'x + u_3x \\ v_1 + a'x + c'y - u_3y \\ 2c \end{bmatrix} \tag{9}$$

Note that though we use the common linear strain tensor definition, the model has already accounted for geometric nonlinearity by factoring out the rotation in (5). Invoking the conventional generalized Hooke's law for an elastic material in 3D gives the elastic energy density U^+ at a point in the material

$$U^+ = \frac{1}{2}\underline{\boldsymbol{\epsilon}}^\top \mathbf{K}\underline{\boldsymbol{\epsilon}} \tag{10}$$

where the 2 stiffness matrix is

$$\mathbf{K} = \left[\begin{array}{ccc|c} M & \lambda & \lambda & \\ \lambda & M & \lambda & \mathbf{0}_{3\times3} \\ \lambda & \lambda & M & \\ \hline \multicolumn{3}{c|}{\mathbf{0}_{3\times3}} & G\mathbf{I}_{3\times3} \end{array}\right] \tag{11}$$

where G is the shear modulus, λ is the first Lamé parameter, and M is the P-wave modulus. In terms of Young's modulus E and Poisson's ratio ν, these constants are

$$\begin{aligned} \lambda &= \frac{E\nu}{(1+\nu)(1-2\nu)}, \quad M = \frac{E(1-\nu)}{(1+\nu)(1-2\nu)} \\ G &= \frac{E}{2(1+\nu)} \end{aligned} \tag{12}$$

IEEE Robotics and Automation Letters (RA-L) paper, presented at ICRA 2026, Vienna, Austria. Cite as RA-L paper.

Note that such a hyperelastic potential energy function implicitly defines a stress-strain relationship, which ultimately gives rise to generalized internal forces. Separating the strain vector into its constant terms and terms that depend linearly on x and y, we have

$$\underline{\boldsymbol{\epsilon}} = \boldsymbol{\epsilon}_0 + \boldsymbol{\epsilon}_x x + \boldsymbol{\epsilon}_y y \tag{13}$$

where

$$\boldsymbol{\epsilon}_0 = \begin{bmatrix} a-1 \\ b-1 \\ v_3-1 \\ v_2 \\ v_1 \\ 2c \end{bmatrix} \quad \boldsymbol{\epsilon}_x = \begin{bmatrix} 0 \\ 0 \\ -u_2 \\ c'+u_3 \\ a' \\ 0 \end{bmatrix} \quad \boldsymbol{\epsilon}_y = \begin{bmatrix} 0 \\ 0 \\ u_1 \\ b' \\ c'-u_3 \\ 0 \end{bmatrix} \tag{14}$$

Integrating the energy density over the cross-sectional area A then gives the elastic energy per unit length along the rod:

$$U' = \frac{1}{2} \iint_A (\boldsymbol{\epsilon}_0 + \boldsymbol{\epsilon}_x x + \boldsymbol{\epsilon}_y y)^\top \mathbf{K} (\boldsymbol{\epsilon}_0 + \boldsymbol{\epsilon}_x x + \boldsymbol{\epsilon}_y y) \, dA \tag{15}$$

If the cross section axes corresponding to the variables x and y are centered such that $x = 0$ and $y = 0$ coincides with the the centroid of the cross section, and if either x or y is an axis of symmetry, then the linear and mixed product terms in the integrand yield zero after integration over the area. This leaves us with

$$U' = \frac{1}{2} \left(\boldsymbol{\epsilon}_0^\top \mathbf{K} \boldsymbol{\epsilon}_0 A + \boldsymbol{\epsilon}_x^\top \mathbf{K} \boldsymbol{\epsilon}_x I_y + \boldsymbol{\epsilon}_y^\top \mathbf{K} \boldsymbol{\epsilon}_y I_x \right) \tag{16}$$

where A is the undeformed cross-sectional area in the undeformed state, and $I_x = \iint_A y^2 dA$ and $I_y = \iint_A x^2 dA$ are the second area moments of the undeformed cross section (and note that $I_z = I_x + I_y$ will be used below). To gain physical intuition about the constitutive law and compare it to others, we can expand it as

$$\begin{aligned} U' = & \frac{1}{2} \Big(GAv_1^2 + GAv_2^2 + 4GAc^2 \\ & + MI_x u_1^2 + MI_y u_2^2 + GI_z u_3^2 \\ & + A \begin{bmatrix} a-1 \\ b-1 \\ v_3-1 \end{bmatrix}^\top \begin{bmatrix} M & \lambda & \lambda \\ \lambda & M & \lambda \\ \lambda & \lambda & M \end{bmatrix} \begin{bmatrix} a-1 \\ b-1 \\ v_3-1 \end{bmatrix} \\ & + GI_y a'^2 + GI_x b'^2 + GI_z c'^2 \\ & + 2G(I_y - I_x) c' u_3 \Big) \end{aligned} \tag{17}$$

C. Comparison to Cosserat Theory

The conventional Cosserat constitutive laws give the energy per unit length as

$$\begin{aligned} U' = & \frac{1}{2} \Big(GAv_1^2 + GAv_2^2 + EA(v_3 - 1)^2 \\ & + EI_x u_1^2 + EI_y u_2^2 + GI_z u_3^2 \Big) \end{aligned} \tag{18}$$

We can compare this to (17) to gain physical insight. Observe that the first two scalar terms of (17) account for the shear energy and are identical to the conventional Cosserat shear energy terms. The third term of (17) accounts for additional shear energy associated with the shearing of the cross section, which is parameterized by c. On the second line of (17), we have the conventional Cosserat bending and torsion energies, but in the bending terms the P-Wave modulus M appears in the place of Young's modulus. We will discuss this in the next section. The matrix-vector quadratic product in the third line gives the energy associated with the combined effect of material compression or elongation in all directions, and the Poisson coupling between the x, y, and s dimensions is clearly present. The bottom-right entry in the matrix yields the term $MA(v_3 - 1)^2$, which corresponds to elongation energy in the conventional Cosserat model, again with M appearing in place of E. The fourth line of (17) describes additional shear energy which penalizes the rate of change of the cross-sectional deformation with respect to s. Note that these terms are dependent on the second-area moments, in contrast to the other shear terms in the first line which are dependent on the area. The last line of (17) describes an additional shear energy that couples torsion u_3 to c' in the case where $I_x \neq I_y$. We note that no terms of this kind appeared in [24].

Thus, linearizing the deformation gradient in the rotated frame gave us an energy integrand which is an intuitive quadratic function of the the state variables with clear analogy to the standard Cosserat model. A further benefit is that no more geometric information about the cross section is needed beyond what is already required in the standard Cosserat model (i.e. A, I_x, and I_y).

D. Stiffness Corrections

Besides the presence of additional terms, the energy expression above differs from the standard Cosserat energy by the presence of M in place of E in the two bending terms and the elongation term as noted above. For a material with a Poisson's ratio of $\nu = 0.3$, $M \approx 1.35E$, while for a nearly incompressible material ($\nu = 0.49$), $M \approx 17E$.

We can easily show that this energy generates the correct stretch and Poisson effect associated with an internal axial stretch force F_z. Considering only the coupled elongation and cross-sectional term,

$$U_e' = \frac{1}{2} A \begin{bmatrix} a-1 \\ b-1 \\ v_3-1 \end{bmatrix}^\top \begin{bmatrix} M & \lambda & \lambda \\ \lambda & M & \lambda \\ \lambda & \lambda & M \end{bmatrix} \begin{bmatrix} a-1 \\ b-1 \\ v_3-1 \end{bmatrix} \tag{19}$$

the associated internal force is then

$$\mathbf{F}_e = \nabla U_e' = A \begin{bmatrix} M & \lambda & \lambda \\ \lambda & M & \lambda \\ \lambda & \lambda & M \end{bmatrix} \begin{bmatrix} a-1 \\ b-1 \\ v_3-1 \end{bmatrix} \tag{20}$$

Solving for a, b, and v_3 in the case of a pure axial force $\mathbf{F}_e = [0 \quad 0 \quad F_z]^\top$, we observe the equation produces the correct strains and stiffness:

$$\begin{bmatrix} a-1 \\ b-1 \\ v_3-1 \end{bmatrix} = \frac{1}{EA} \begin{bmatrix} -\nu \\ -\nu \\ 1 \end{bmatrix} F_z \tag{21}$$

In the case of bending, a similar Poisson coupling should occur physically. During bending, one side of the material is axially compressed while the other is in axial tension, leading to cross-sectional expansion on the compressed side and contraction on the other (causing a square cross section to be transformed into a roughly trapezoidal shape). However, the parameterized cross-sectional deformation a, b, and c cannot represent this behavior by themselves. To model this behavior explicitly,

IEEE Robotics and Automation Letters (RA-L) paper, presented at ICRA 2026, Vienna, Austria. Cite as RA-L paper.

we can incorporate additional cross-sectional deformation modes (as we do later in Section II-F) which increases model complexity. However, since we know that during bending the cross section will deform in this way that has not been explicitly parameterized, and since we know that allowing further cross-sectional modes would reduce the effective bending stiffnesses to EI_x and EI_y, we can simply replace the M with E in the two bending stiffness terms in (17). This modification will cause the model to display the correct bending stiffness, even without explicitly modeling the more complex cross-sectional modes associated with bending.

In the case of torsion in the Cosserat model, non-circular cross sections have lower torsional rigidity than GI_z because of non-circular shear lines. In standard mechanics approaches for non-circular cross sections, this is resolved by multiplying the polar moment of inertia I_z by a correction factor η that depends on the specific cross section of the rod. For a square cross section, this correction factor is $\eta = 0.846$ [27]. In our model, we can incorporate this by multiplying the I_z terms by η. Implementing both bending and torsion stiffness corrections then gives the following modified energy per unit length along the rod:

$$\begin{aligned} U' =& \frac{1}{2}\Big(GAv_1^2 + GAv_2^2 + 4GAc^2 \\ &+ EI_x u_1^2 + EI_y u_2^2 + \eta GI_z u_3^2 \\ &+ A \begin{bmatrix} a-1 \\ b-1 \\ v_3-1 \end{bmatrix}^\top \begin{bmatrix} M & \lambda & \lambda \\ \lambda & M & \lambda \\ \lambda & \lambda & M \end{bmatrix} \begin{bmatrix} a-1 \\ b-1 \\ v_3-1 \end{bmatrix} \\ &+ GI_y a'^2 + GI_x b'^2 + \eta GI_z c'^2 \\ &+ 2G(I_y - I_x)c' u_3 \Big) \end{aligned} \tag{22}$$

E. A Geometrically Nonlinear Constitutive Law

The deformation gradient in (6) is nonlinear in the deformation parameters because it depends on the product $\widehat{\mathbf{u}}\mathbf{C}$. We linearized $\mathbf{D}$ in (7) for simplicity, but we can obtain a more exact constitutive law without linearizing $\mathbf{D}$. Proceeding with this strategy, we again identify the parts of the strain vector,

$$\boldsymbol{\epsilon}_0 = \begin{bmatrix} a-1 \\ b-1 \\ v_3-1 \\ v_2 \\ v_1 \\ 2c \end{bmatrix} \quad \boldsymbol{\epsilon}_x = \begin{bmatrix} 0 \\ 0 \\ cu_1 - au_2 \\ c' + au_3 \\ a' - cu_3 \\ 0 \end{bmatrix} \quad \boldsymbol{\epsilon}_y = \begin{bmatrix} 0 \\ 0 \\ bu_1 - cu_2 \\ b' + cu_3 \\ c' - bu_3 \\ 0 \end{bmatrix} \tag{23}$$

and observe that the energy expression (16) is still valid with these nonlinear strain expressions subbed in. Expanding the result in a similar form to (17), and including the bending stiffness correction (swapping MI for EI) and the torsional stiffness correction factor η from the previous section:

$$\begin{aligned} U' =& \frac{1}{2}\Big(GAv_1^2 + GAv_2^2 + 4GAc^2 \\ &+ \mathbf{u}^\top \begin{bmatrix} k_{11} & k_{12} & 0 \\ k_{12} & k_{22} & 0 \\ 0 & 0 & \eta k_{33} \end{bmatrix} \mathbf{u} \\ &+ A \begin{bmatrix} a-1 \\ b-1 \\ v_3-1 \end{bmatrix}^\top \begin{bmatrix} M & \lambda & \lambda \\ \lambda & M & \lambda \\ \lambda & \lambda & M \end{bmatrix} \begin{bmatrix} a-1 \\ b-1 \\ v_3-1 \end{bmatrix} \\ &+ GI_y a'^2 + GI_x b'^2 + \eta GI_z c'^2 \\ &+ 2G((ac' - a'c)I_y - (bc' - b'c)I_x)u_3 \end{aligned} \tag{24}$$

where

$$\begin{aligned} k_{11} &= E(I_x b^2 + I_y c^2),\ k_{12} = -E(I_y ac + I_x bc) \\ k_{22} &= E(I_y a^2 + I_x c^2),\ k_{33} = G(I_y a^2 + I_x b^2 + I_z c^2) \end{aligned} \tag{25}$$

Note that the torsional stiffness correction factor η is applied to k_{33} as this is the torsional stiffness. Comparing the result to (22) we see that the bending and torsion stiffness matrix is no longer diagonal, and its elements depend on a b and c. This dependence can be interpreted as a modification of second area moments according to the cross section deformation. Furthermore, the coupling between torsion and cross-sectional shear in the last line is now more complex.

F. Parameterizing Linear Modes of Deformation

As mentioned in the previous section, the parameters $a(s)$, $b(s)$, and $c(s)$ that are constant throughout the cross section of the rod at a given s are not able to fully capture the cross-sectional deformation modes that occur during bending, where one side of the cross section contracts and the opposite side stretches. This results in an unnaturally stiff response to bending, especially for materials with high Poisson's ratio. Rather than substituting E for M in the bending stiffness terms, we can explicitly parameterize these trapezoidal modes of deformation (as explored in [23]) in our energy expression by allowing $a(s)$, $b(s)$, $c(s)$ to also vary over the cross section as linear functions of x and y for a given s. To avoid notational confusion, we adopt new symbols for the cross section modes (α, β, γ) when adopting this expanded model

$$\begin{aligned} \alpha(x, y, s) &= a_0(s) + a_x(s)x + a_y(s)y \\ \beta(x, y, s) &= b_0(s) + b_x(s)x + b_y(s)y \\ \gamma(x, y, s) &= c_0(s) + c_x(s)x + c_y(s)y \end{aligned} \tag{26}$$

By parameterizing in this way, we allow parallel lines in the original cross section to no longer be parallel in the deformed cross section. Following the same procedure outlined above, we can again derive an equation for the energy per unit length in the rod. We start by computing $\partial\mathbf{x}/\partial\mathbf{X}$, substituting the equations for α, β and γ in $\mathbf{C}(s)$ in place of a, b, and c, respectively. Then, we factor out $\mathbf{R}$ resulting in a new matrix $\mathbf{D} = [\mathbf{D}_1 \ \ \mathbf{D}_2 \ \ \mathbf{D}_3]$ with the following columns:

$$\begin{aligned} \mathbf{D}_1 &= \begin{bmatrix} \alpha + a_x x + c_x y \\ \gamma + c_x x + b_x y \\ 0 \end{bmatrix} \quad \mathbf{D}_2 = \begin{bmatrix} \gamma + a_y x + c_y y \\ \beta + c_y x + b_y y \\ 0 \end{bmatrix} \\ \mathbf{D}_3 &= \begin{bmatrix} v_1 + \alpha' x + \gamma' y - \beta u_3 y - \gamma u_3 x \\ v_2 + \beta' y + \gamma' x + \alpha u_3 x + \gamma u_3 y \\ v_3 - (\alpha u_2 - \gamma u_1)x + (\beta u_1 - \gamma u_2)y \end{bmatrix} \end{aligned} \tag{27}$$

where α, β, γ, α', β', and γ' are implicit functions of x, y, and s, and $\mathbf{u}$ and $\mathbf{v}$ are implicit functions of s.

Using the definition of the strain tensor in (8) results in a strain vector with constant terms and terms in x, y, xy, x^2 and y^2. Thus, we can decompose the strain vector into a linear combination of terms as done in (13):

$$\underline{\boldsymbol{\epsilon}} = \boldsymbol{\epsilon}_0 + \boldsymbol{\epsilon}_x x + \boldsymbol{\epsilon}_y y + \boldsymbol{\epsilon}_{xy} xy + \boldsymbol{\epsilon}_{x^2} x^2 + \boldsymbol{\epsilon}_{y^2} y^2 \tag{28}$$

IEEE Robotics and Automation Letters (RA-L) paper, presented at ICRA 2026, Vienna, Austria. Cite as RA-L paper.

where

$$\boldsymbol{\epsilon}_0 = \begin{bmatrix} a_0-1 \\ b_0-1 \\ v_3-1 \\ v_2 \\ v_1 \\ 2c_0 \end{bmatrix} \quad \boldsymbol{\epsilon}_x = \begin{bmatrix} 2a_x \\ b_x+c_y \\ u_1c_0-a_0u_2 \\ c_0'+a_0u_3 \\ a_0'-c_0u_3 \\ 3c_x+a_y \end{bmatrix} \quad \boldsymbol{\epsilon}_y = \begin{bmatrix} c_x+a_y \\ 2b_y \\ b_0u_1-c_0u_2 \\ b_0'+c_0u_3 \\ c_0'-b_0u_3 \\ b_x+3c_y \end{bmatrix}$$

$$\boldsymbol{\epsilon}_{x^2} = \begin{bmatrix} 0 \\ 0 \\ c_xu_1-a_xu_2 \\ c_x'+a_xu_3 \\ a_x'-c_xu_3 \\ 0 \end{bmatrix} \quad \boldsymbol{\epsilon}_{y^2} = \begin{bmatrix} 0 \\ 0 \\ b_yu_1-c_yu_2 \\ b_y'+c_yu_3 \\ c_y'-b_yu_3 \\ 0 \end{bmatrix}$$

$$\boldsymbol{\epsilon}_{xy} = \begin{bmatrix} 0 \\ 0 \\ c_yu_1-a_yu_2+b_xu_1-c_xu_2 \\ b_x'+c_y'+a_yu_3+c_xu_3 \\ a_y'+c_x'-b_xu_3-c_yu_3 \\ 0 \end{bmatrix} \tag{29}$$

With the new expression for the strain vector $\underline{\boldsymbol{\epsilon}}$, the product evaluated in the cross-sectional area integral $\underline{\boldsymbol{\epsilon}}^\top \mathbf{K} \underline{\boldsymbol{\epsilon}}$ now contains additional terms up to fourth-order in x and y. With the same assumptions as before, namely that the (x, y) origin coincides with the cross-sectional area centroid and that either x or y is an axis of symmetry, the terms with odd powers in x or y are zero after integration over the area. This leaves

$$\begin{aligned} U' = \frac{1}{2}\Big(& \boldsymbol{\epsilon}_0^\top \mathbf{K} \boldsymbol{\epsilon}_0 A + \boldsymbol{\epsilon}_x^\top \mathbf{K} \boldsymbol{\epsilon}_x I_y + \boldsymbol{\epsilon}_y^\top \mathbf{K} \boldsymbol{\epsilon}_y I_x \\ & + 2\boldsymbol{\epsilon}_0^\top \mathbf{K} \boldsymbol{\epsilon}_{x^2} I_y + 2\boldsymbol{\epsilon}_0^\top \mathbf{K} \boldsymbol{\epsilon}_{y^2} I_x \\ & + 2\boldsymbol{\epsilon}_{x^2}^\top \mathbf{K} \boldsymbol{\epsilon}_{y^2} Q_{xy} + \boldsymbol{\epsilon}_{xy}^\top \mathbf{K} \boldsymbol{\epsilon}_{xy} Q_{xy} \\ & + \boldsymbol{\epsilon}_{x^2}^\top \mathbf{K} \boldsymbol{\epsilon}_{x^2} Q_y + \boldsymbol{\epsilon}_{y^2}^\top \mathbf{K} \boldsymbol{\epsilon}_{y^2} Q_x \Big) \end{aligned} \tag{30}$$

where we define $Q_x = \iint\limits_A y^4 dA$, $Q_y = \iint\limits_A x^4 dA$, and $Q_{xy} = \iint\limits_A x^2 y^2 dA$. We note that these integrals are straightforward to compute for common cross sections. The bending stiffness correction is not needed because the additional parameterized deformation modes should reduce the effective stiffness to something closer to EI. However, the torsional correction factor is still necessary and can be incorporated in the same manner as in previous sections.

III. Implementation

A. Minimization of Total Potential Energy

Let $\mathbf{z} = [a \;\; b \;\; c \;\; a' \;\; b' \;\; c' \;\; \mathbf{v}^\top \;\; \mathbf{u}^\top]^\top$. For a cantilevered rod with a fixed end at $s = 0$ and subject to some point forces $\mathbf{f}_i$ at locations $\mathbf{X}_i$, we can then cast the mechanics problem in the following form via the principle of minimum total potential energy.

$$\begin{aligned} \underset{\mathbf{z}(s)}{\text{minimize}} \quad & \boldsymbol{\Pi} = \int_0^L U'(\mathbf{z}, s) ds - \sum \mathbf{f}_i^\top (\mathbf{x}(\mathbf{X}_i) - \mathbf{X}_i) \\ \text{subject to} \quad & \\ \mathbf{z}_{1-3}' = & \mathbf{z}_{4-6}, \quad \mathbf{z}_{1-3}(0) = [1 \;\; 1 \;\; 0]^\top \\ \mathbf{R}' = & \mathbf{R}\widehat{\mathbf{u}}, \quad \mathbf{R}(0) = \mathbf{I} \\ \mathbf{p}' = & \mathbf{R}\mathbf{v}, \quad \mathbf{p}(0) = \mathbf{0} \end{aligned} \tag{31}$$

and where $\mathbf{x}(\mathbf{X}_i)$ is calculated as written in (1).

In practice, we discretize the length L of the rod into n nodes with uniform spacing $h = L/(n-1)$. The cross-sectional deformation parameters a, b, and c are defined at each of these n nodes, while the Cosserat parameters $\mathbf{v}$ and $\mathbf{u}$ are defined at each of the $(n-1)$ midpoints between the nodes (see Figure 1), resulting in $3n + 6(n-1)$ total states.

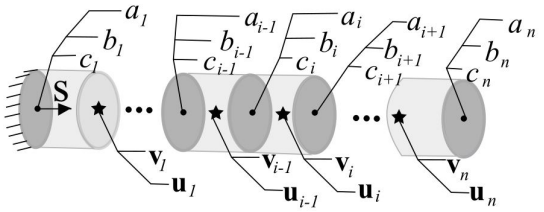

Fig. 1. Locations of state variables a, b, c, $\mathbf{v}$, and $\mathbf{u}$ are shown for a rod discretized into n nodes.

The potential energy per unit length U' inside each of the $(n-1)$ rod segments is taken to be constant, so the integral expression in (31) evaluates to the summation $\sum_{i=1}^{n-1} hU_i'$ where U_i' is the energy per unit length for rod segment i (i.e. the $U'(s)$ evaluated at the midpoint between node i and node $i+1$). The cross-sectional deformation parameters a, b and c at the rod segment i are the averages between nodes i and $i+1$. The derivative a' at rod segment i is simply $a' = (a_{i+1} - a_i)/h$, with similar expressions for b' and c'.

For the expanded model that parameterizes linear cross-sectional deformation modes, the states $\mathbf{z}$ and their constraints become

$$\begin{aligned} \mathbf{z} &= [\mathbf{a}^\top \;\; \mathbf{b}^\top \;\; \mathbf{c}^\top \;\; \mathbf{a}'^\top \;\; \mathbf{b}'^\top \;\; \mathbf{c}'^\top \;\; \mathbf{v}^\top \;\; \mathbf{u}^\top]^\top \\ \mathbf{z}_{1-9}' &= \mathbf{z}_{10-18} \\ \mathbf{z}_{1-9}(0) &= [1 \;\; 0 \;\; 0 \;\; 1 \;\; 0 \;\; 0 \;\; 0 \;\; 0 \;\; 0]^\top, \end{aligned} \tag{32}$$

where $\mathbf{a} = [a_0 \;\; a_x \;\; a_y]^\top$, $\mathbf{b} = [b_0 \;\; b_x \;\; b_y]^\top$, and $\mathbf{c} = [c_0 \;\; c_x \;\; c_y]^\top$.

B. Soft Robot Actuation

Consider a pressure-driven soft robot with an embedded chamber whose centroid is located at $[x_a \;\; y_a]^\top$ in the undeformed cross section, with area $\Gamma(s)$ before deformation. The volume of the chamber V after deformation can be calculated by integrating

$$\begin{aligned} V' &= |D(s, x_a, y_a)|\Gamma(s) \\ &= (ab - c^2)(v_3 - u_2 x_a + u_1 y_a)\Gamma(s) \end{aligned} \tag{33}$$

over the length of the chamber. We can add the actuation energy of the pressurized fluid (assuming adiabatic compression) to the total potential energy in (31) as the product of applied pressure and volume. Alternatively, if the fluid is incompressible, and the fluid volume is dictated by a fluidic actuator, we can apply an additional volume constraint to the constraint set in (31) and solve the system using a constrained optimization algorithm.

A similar approach can be taken to model tendon or cable actuation. If the tendon path is defined by the tendon channel's location in the cross section as function of s:

$$\boldsymbol{\rho}_t(s) = [\rho_x(s) \;\; \rho_y(s) \;\; 0]^\top$$

then the global frame tendon position at s is

$$\mathbf{p}_t(s) = \mathbf{p}(s) + \mathbf{R}(s)\mathbf{C}(s, \rho_x, \rho_y)\boldsymbol{\rho}(s) \tag{34}$$

IEEE Robotics and Automation Letters (RA-L) paper, presented at ICRA 2026, Vienna, Austria. Cite as RA-L paper.

and the total tendon length ℓ_t is given by integrating

$$\ell_t' = \mathbf{v} + \hat{\mathbf{u}}\mathbf{C}\boldsymbol{\rho} + \mathbf{C}'\boldsymbol{\rho} + \mathbf{C}\boldsymbol{\rho}' \tag{35}$$

where $\mathbf{C}'$ involves appropriate use of the chain rule if the expanded model is used. Similar to fluid actuation, tendon actuation can be modeled by adding $\tau\ell_t$ to the total energy if the tendon tension is dictated, or by adding a length constraint to the constraint set in (31) if the length is dictated.

IV. Simulation Comparisons

We performed simulation experiments to verify the proposed Cosserat models against a reference finite-element simulation. The models were implemented in C++ with L-BFGS used to solve the optimization problem in (31). The gradient of the strain energy U with respect to the state variables is computed analytically while the gradient of the applied force position $\mathbf{x}(\mathbf{X_i})$ is computed via finite differences. The constraints in (31) are "embedded" by numerically integrating the differential equations before computing the objective function. For each experiment, a convergence analysis determined the number of nodes to achieve converged tip displacements. Increasing the number of nodes beyond this point has diminishing returns with respect to the agreement with finite element simulations, as some cross-sectional deformation modes and out-of-plane warping are not captured by our model. Fewer nodes may also be used while still providing acceptable accuracy, though there will be more disagreement with finite element simulations due to discretization error.

The reference simulations are three-dimensional finite element method (FEM) solves from Inventor Nastran, with a nonlinear solver, an isotropic material, and quadratic tetrahedral elements. Convergence analyses are performed to select appropriate levels of mesh discretization that are within one percent of the converged tip displacement. Material and mesh parameters will be specified for each experiment below.

For the experiments that follow, we quantify error with the average per-vertex error between a rod model and a FEM result. For each vertex in the FEM mesh we calculate the error between it and the corresponding location in the rod model, and we average the errors across the mesh. Computation times are reported for a single static solve on a single core of a Ryzen 9 9950X CPU, averaged across 20 trials.

A. Axial Stretching

A cylinder with $0.5\,\mathrm{m}$ radius and $2\,\mathrm{m}$ height is fixed at its base and loaded with a tensile or compressive force. The cylinder has material properties $E = 1 \times 10^5\,\mathrm{Pa}$ and $\nu = 0.49$. Its top surface is constrained to be parallel to the ground with cross-sectional deformation disallowed. $50\,\mathrm{kN}$ and $20\,\mathrm{kN}$ tensile forces are applied, and $5\,\mathrm{kN}$ and $15\,\mathrm{kN}$ compressive forces are applied. The cylinder is discretized into 21 nodes and simulated with the nonlinear constitutive model (24), and an equivalent FEM simulation with 27193 elements is performed. Figure 2 compares our model against the FEM results, and a quantitative comparison is made in Table I with elongation error and average per-vertex error. The results show reasonable agreement. The optimization for the standard Cosserat rod model is faster ($\sim$3 ms), but its average per-vertex error is 5 times higher than our extended Cosserat model.

TABLE I
Comparison of Our Model and FEM for Axial Stretching

Load [kN]	Z-Coordinate % Difference	Avg Per-Vertex Error [m]	Compute Time [ms]
50	4.3%	0.0777	54.83
20	0.5%	0.0129	22.94
-5	0.2%	0.0020	8.91
-15	0.9%	0.0097	48.96

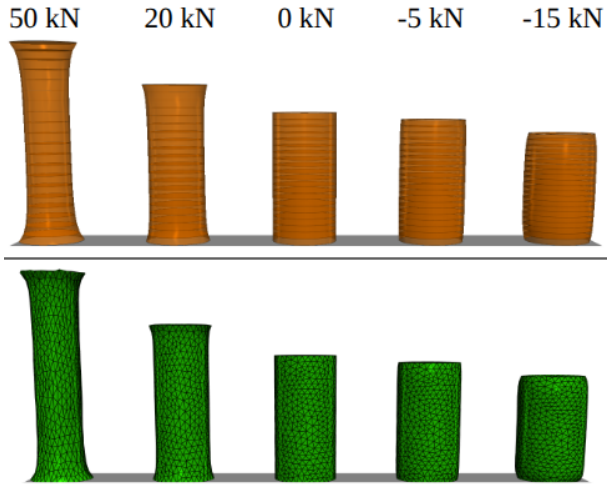

Fig. 2. A cylindrical rod is subjected to a range of axial forces. The top surface is constrained to not deform in the transverse directions. **Top**. The extended Cosserat model of (24) including cross-sectional deformation and axial elongation. **Bottom**. 3D nonlinear finite element analysis results for the same loading conditions. Good agreement is seen between our model and the FEM results in terms of cross-sectional deformation and axial elongation.

B. Bending

A $2\,\mathrm{m}$ long, $1\,\mathrm{m} \times 0.5\,\mathrm{m}$ rod with $E = 1 \times 10^5\,\mathrm{Pa}$ and a fixed base is subjected to a transverse tip load of $500\,\mathrm{N}$. The rod is discretized into 20 nodes. Four variations of our model are simulated with the same geometry, loading, and boundary conditions: (A) the linearized constitutive law without the bending stiffness correction (i.e. it uses MI instead of EI) (17), (B) the linearized constitutive law with the bending stiffness correction (22), (C) the nonlinear constitutive law with the bending stiffness correction (24), and (D) the nonlinear constitutive law that includes linear cross-sectional deformation modes (30). The models are compared to a reference finite element simulation with 17244 elements.

Results for two values of Poisson's ratio, $\nu = 0.3$ and $\nu = 0.49$, are shown in Figure 3. Deformed cross sections at $s = 0.2\,\mathrm{m}$ are displayed below their respective rod model simulations. Table II displays tip errors compared to the FEM result in the direction of bending (Y-axis) and in the vertical direction (Z-axis), as well as the average per-vertex error and computation time. For a standard Cosserat rod with 20 nodes, the optimization takes $4.12\,\mathrm{ms}$ and $3.95\,\mathrm{ms}$ for $\nu = 0.3$ and $\nu = 0.49$, with an average per-vertex error of $0.0066\,\mathrm{m}$

IEEE Robotics and Automation Letters (RA-L) paper, presented at ICRA 2026, Vienna, Austria. Cite as RA-L paper.

TABLE II
COMPARISON OF OUR MODELS AND FEM FOR BENDING

$E = 1 \times 10^5$ Pa, $\nu = 0.3$				
Model	Tip Y % Diff	Tip Z % Diff	Avg Per-Vertex Error [m]	Compute Time [ms]
A	16.5%	5.98%	0.0751	23.63
B	0.10%	0.18%	0.00658	20.40
C	0.20%	0.41%	0.00973	8.09
D	1.30%	0.41%	0.00823	73.54
$E = 1 \times 10^5$ Pa, $\nu = 0.49$				
Model	Tip Y % Diff	Tip Z % Diff	Avg Per-Vertex Error [m]	Compute Time [ms]
A	86.2%	16.6%	0.337	16.46
B	4.36%	1.64%	0.0298	35.24
C	5.40%	1.75%	0.0337	22.81
D	4.67%	1.64%	0.0250	134.57

and $0.0298\,\mathrm{m}$, respectively. Our model without the bending stiffness correction (Model A) is stiffer and less accurate than the other models, especially for $\nu = 0.49$ since for this case, $M \approx 17E$. With the bending stiffness correction included, both the linearized constitutive model (Model B) and the nonlinear constitutive model (Model C) align well with the FEM results. The model that parameterizes linear cross-sectional deformation modes (Model D) is also accurate, but required far more compute time. Figure 3 shows that while model D captured the trapezoidal shape of the deformed cross section (as also shown in [23]), and has the lowest average per-vertex error in the $\nu = 0.49$ case, it did not capture the slightly curved edges seen in the FEM cross section.

C. Torsion

In Figure 4, a square $2\,\mathrm{m}$ rod with $0.5\,\mathrm{m} \times 0.5\,\mathrm{m}$ cross section, $E = 1 \times 10^5\,\mathrm{Pa}$ and $\nu = 0.49$ is subjected to a $3000\,\mathrm{N\,m}$ torsional load. We used the nonlinear constitutive model (24), 21 nodes, and two values of the torsional correction parameter η are tested. Model A uses $\eta = 1$ (no correction) while Model B uses $\eta = 0.846$ (correction factor for square cross sections). The angular deflection ϕ is compared to the reference FEM simulation with and 14328 elements. Using $\eta = 1$ results a 12% undershoot in angular deflection compared to the FEM while using $\eta = 0.846$ results in a 5% overshoot.

D. Peristaltic Worm-Inspired Robot

To illustrate the usefulness of cross-section deformation modeling in soft robotics, we developed a model of an earthworm-inspired robot, which consists of a circular rod with embedded pairs of pneumatic actuators along the length of the rod. Inflating the embedded actuators causes cross-sectional deformation (which is incorporated in the energy minimization as described in Section III-B), and a pressure differential across a pair of actuators creates a bending moment over the nodes spanned by the actuators. We emphasize that the modeling of such a robot is not possible using the traditional Cosserat model. The design of a robot with two pairs of actuators is shown in Figure 5.

A pipe-crawling robot (Figure 5, bottom) has many actuator pairs that inflate and deflate in peristaltic waves. The cross-sectional deformation of an inflated segment is constrained radially by the pipe, and the inflated segment becomes fixed in the pipe due to friction, resulting in forward motion. Constraints for fixing nodal poses to the pipe are satisfied using Alglib's sparse filter-based SQP solver [28].

A ground-crawling robot (Figure 5, top) operates under the same principles as the pipe-crawling robot, but without the

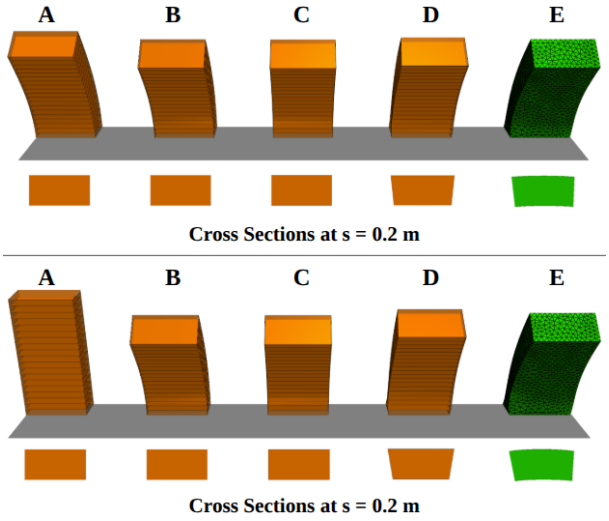

Fig. 3. A $2\,\mathrm{m}$ long rectangular rod is subjected to a transverse tip load. Simulation results are shown above cross-sections taken at $s = 0.2\,\mathrm{m}$. The top row simulates a material with $\nu = 0.3$, and the bottom row simulates a nearly incompressible material with $\nu = 0.49$. The models from left to right are: **A** the linearized model without stiffness correction (17), **B** the linearized model with stiffness correction 22, **C** the nonlinear model with stiffness correction (24), **D** the nonlinear model with additional cross section modes (30), and **E** the 3D nonlinear finite element model. Note the trapezoidal deformation mode captured by Model D, and the warping of the finite element cross-section not captured by Model D.

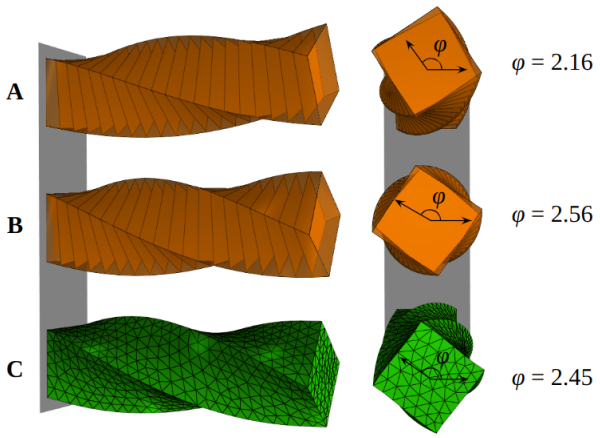

Fig. 4. A square rod is subjected to a large torsional load. The models from left to right are: **A** the nonlinear constitutive model (24) no torsional stiffness correction factor ($\eta = 1$), **B** the nonlinear constitutive model (24) with standard torsional correction factor ($\eta = 0.846$), and **C** the 3D nonlinear finite element model. Note that cross sectional deformation is happening in both models, due to the coupling of shear and torsion.

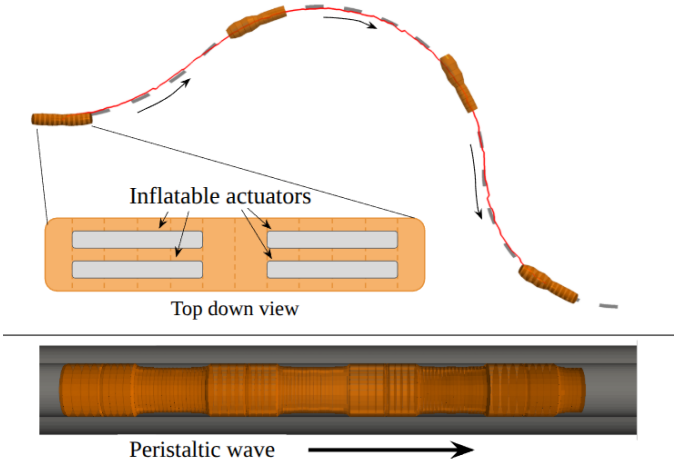

Fig. 5. **Top.** A peristaltic robot with two pairs of inflatable actuators, simulated with $N = 13$ nodes, performs an optimization over the pressure differentials in each pair of actuators to minimize path error at each step. The dashed gray line is the desired path and the red line is the path followed by the center of the robot. The inset shows the structure of the robot from a top down view. **Bottom.** A soft robot with 18 center-aligned actuators and $N = 109$ nodes crawls down a pipe using a peristaltic gait.

radial constraints. To simplify contact modeling, any actuator segment that is in contact with the ground is assumed to be fixed in both position and orientation. Model-based path-following control is shown in (Figure 5, top). Each time an actuator pair is inflated, we select the pressure differentials for each actuator pair to minimize a weighted sum of path tangent error and position error for all actuators in the robot. The optimal pressures are then applied to the robot for the current inflation phase, and the process is repeated. Both scenarios in Figure 5 are shown in the supplemental video.

V. Conclusion

In this work, we have presented an extension to Cosserat rod theory that efficiently incorporates cross-sectional deformation, with application to soft robotics. We identify energy terms associated with cross-section deformation, in addition to the conventional Cosserat energy terms and identify previously unforseen coupling terms. We further investigate using various levels of approximation for the energy density and the inclusion of additional cross section modes. We showed how to incorporate common soft robot actuation methods into the model, and verified the agreement of the approach against a reference nonlinear solution using nonlinear finite elements. This work can be useful to more accurately describe the behavior and deformed shape of soft robots in a variety of applications.

References

[1] C. Armanini, F. Boyer, A. T. Mathew, C. Duriez, and F. Renda, "Soft robots modeling: A structured overview," *IEEE Transactions on Robotics*, vol. 39, no. 3, pp. 1728–1748, 2023.

[2] R. Rafiee and R. M. Moghadam, "On the modeling of carbon nanotubes: a critical review," *Composites Part B: Engineering*, vol. 56, pp. 435–449, 2014.

[3] T. Guillon, Y. Dumont, and T. Fourcaud, "A new mathematical framework for modelling the biomechanics of growing trees with rod theory," *Mathematical and Computer Modelling*, vol. 55, no. 9-10, pp. 2061–2077, 2012.

[4] D. K. Pai, "Strands: Interactive simulation of thin solids using cosserat models," in *Computer graphics forum*, vol. 21, pp. 347–352, Wiley Online Library, 2002.

[5] J. T. Miller, A. Lazarus, B. Audoly, and P. M. Reis, "Shapes of a suspended curly hair," *Physical review letters*, vol. 112, no. 6, p. 068103, 2014.

[6] S. S. Antman, "General theories of rods," *Nonlinear Problems of Elasticity*, pp. 603–658, 2005.

[7] A. E. Green, P. Naghdi, and M. Wenner, "On the theory of rods ii. developments by direct approach," *Proceedings of the Royal Society of London. A. Mathematical and Physical Sciences*, vol. 337, no. 1611, pp. 485–507, 1974.

[8] P. Schegg and C. Duriez, "Review on generic methods for mechanical modeling, simulation and control of soft robots," *Plos one*, vol. 17, no. 1, p. e0251059, 2022.

[9] Tunay, "Spatial continuum models of rods undergoing large deformation and inflation," *IEEE Transactions on Robotics*, vol. 29, no. 2, pp. 297–307, 2013.

[10] J. Till, C. E. Bryson, S. Chung, A. Orekhov, and D. C. Rucker, "Efficient computation of multiple coupled Cosserat rod models for real-time simulation and control of parallel continuum manipulators," in *2015 IEEE International Conference on Robotics and Automation (ICRA)*, pp. 5067–5074, IEEE, 5 2015.

[11] F. Janabi-Sharifi, A. Jalali, and I. D. Walker, "Cosserat rod-based dynamic modeling of tendon-driven continuum robots: A tutorial," *IEEE Access*, vol. 9, pp. 68703–68719, 2021.

[12] E. Cosserat and F. Cosserat, "Sur la théorie de l'élasticité. premier mémoire," in *Annales de la Faculté des sciences de Toulouse: Mathématiques*, vol. 10, pp. I1–I116, 1896.

[13] S. S. Antman, "Jl ericksen's work on cosserat theories of rods and shells," *Journal of Elasticity*, vol. 155, no. 1, pp. 31–40, 2024.

[14] H. Altenbach, M. Bîrsan, and V. A. Eremeyev, "Cosserat-type rods," *Generalized Continua from the Theory to Engineering Applications*, pp. 179–248, 2013.

[15] B. Gorissen, D. Reynaerts, S. Konishi, K. Yoshida, J.-W. Kim, and M. De Volder, "Elastic inflatable actuators for soft robotic applications," *Advanced Materials*, vol. 29, no. 43, p. 1604977, 2017.

[16] A. Arora, A. Kumar, and P. Steinmann, "A computational approach to obtain nonlinearly elastic constitutive relations of special cosserat rods," *Computer Methods in Applied Mechanics and Engineering*, vol. 350, pp. 295–314, 2019.

[17] L. Vu-Quoc and I. Ebcioğlu, "Multilayer shells: Geometrically-exact formulation of equations of motion," *International journal of solids and structures*, vol. 37, no. 45, pp. 6705–6737, 2000.

[18] L. Vu-Quoc and I. Ebcioğlu, "On the physical meaning of the dynamical equations governing geometrically-exact multilayer shells," *Computer methods in applied mechanics and engineering*, vol. 194, no. 21-24, pp. 2363–2384, 2005.

[19] T. Gould and D. A. Burton, "A cosserat rod model with microstructure," *New Journal of Physics*, vol. 8, no. 8, p. 137, 2006.

[20] R. Gonçalves, M. Ritto-Corrêa, and D. Camotim, "A large displacement and finite rotation thin-walled beam formulation including cross-section deformation," *Computer Methods in Applied Mechanics and Engineering*, vol. 199, no. 23-24, pp. 1627–1643, 2010.

[21] M. Rubin, "Cosserat rods," in *Cosserat Theories: Shells, Rods and Points*, pp. 191–310, Springer, 2000.

[22] D. H. Hodges, "A mixed variational formulation based on exact intrinsic equations for dynamics of moving beams," *International journal of solids and structures*, vol. 26, no. 11, pp. 1253–1273, 1990.

[23] E. R. Dasambiagio, P. M. Pimenta, and E. M. Campello, "A finite strain rod model that incorporates general cross section deformation and its implementation by the finite element method," in *Solid Mechanics in Brazil 2009, ABCM symposium series in solid mechanics*, vol. 2, pp. 145–168, 2009.

[24] A. Kumar and S. Mukherjee, "A geometrically exact rod model including in-plane cross-sectional deformation," *Journal of Applied Mechanics*, vol. 78, p. 011010, 10 2010.

[25] A. Kumar, S. Mukherjee, J. T. Paci, K. Chandraseker, and G. C. Schatz, "A rod model for three dimensional deformations of single-walled carbon nanotubes," *International Journal of Solids and Structures*, vol. 48, no. 20, pp. 2849–2858, 2011.

[26] C. Fang, A. Kumar, and S. Mukherjee, "Finite element analysis of single-walled carbon nanotubes based on a rod model including in-plane cross-sectional deformation," *International Journal of Solids and Structures*, vol. 50, no. 1, pp. 49–56, 2013.

[27] U. . Fenster, *Advanced Strength and Applied Elasticity*. Elsevier, 1994.

[28] S. Bokhanov, "Alglib." (www.alglib.net).